



## Research papers

# Influence of concentration-dependent diffusivity on lithium plating: Polarization, stability, and dendrite formation in phase-field simulations

Chi-Jyun Ko<sup>1</sup>, Chen-Ning Tai<sup>1</sup>, Chih-Hung Chen<sup>\*</sup>, Kuo-Ching Chen

*Institute of Applied Mechanics, National Taiwan University, Taipei 10617, Taiwan*

## ARTICLE INFO

## Keywords:

Lithium dendrites  
Limiting current density  
Concentration polarization  
Ionic depletion  
Phase-field method

## ABSTRACT

Lithium dendrite issues significantly impede the development of high-energy-density secondary batteries with a lithium anode. The widely-used classical Sand's limiting current density, predicting lithium dendrite formation during plating, relies on constant diffusivity. However, overlooking realistic ion transport dynamics, like concentration-influenced diffusivity, often results in discrepancies between analytical predictions and experiments. To better understand the origin of the observed inconsistency, our study presents a phase-field method for solving the dynamics of ion transport in electrolytes during anode surface migration in plating. The model integrates the Stewart–Newman diffusivity for concentration-influenced ion transport dynamics and the Butler–Volmer equation for electrochemical kinetics at the anode-electrolyte interface. In addition to phase-field simulations, we performed a steady-state analysis of the concentration distribution in electrolytes, determining the limiting current density. Verification confirms strong agreement between the phase-field model and analytical predictions. Our two-dimensional phase-field simulations further reveal that the varying diffusivity, dependent on concentration, plays a crucial role in plating stability and the resulting lithium morphology. Results of this study provides valuable insights for resolving the observed discrepancies in the onset of lithium dendrite formation between experiments and the classical Sand's formula.

## 1. Introduction

Lithium metal, owing to its high theoretical capacity and low electrode potential, shows promise as an anode material for next-generation high-energy-density secondary batteries [1–4]. However, its high reactivity with electrolytes often leads to unstable plating, causing irregular deposits known as lithium dendrites during battery cycling. The appearance of lithium dendrites presents challenges to the safety and performance of the battery, contributing to increased impedance, reduced energy capacity, shortened lifespan, and the risk of short circuits and cell explosions. Hence, the dendrite formation is a primary issue that needs to be resolved before the commercialization of the batteries coupled with a lithium anode [5,6].

Experiments discovered a strong correlation between dendrite morphology and plating current density. Examples include tip-growing fractal dendrites at high current densities, surface-growing mossy dendrites at intermediate current densities, and root-growing lithium whiskers at low current densities [7–10]. Among these irregular lithium deposits, fractal dendrites present significant safety concerns since their sharp tips and rapid growth can easily penetrate separators [7–12]. The formation of these dendrites is found to be closely related to the

depletion of ions near the anode surface at a current above a certain threshold [7–10].

During plating, continuous consumption of lithium ions at the anode surface, caused by electrochemical reactions such as ion reduction and electrolyte decomposition, results in a considerable decrease in concentration at the anode surface, particularly at high current densities. Whereas the electrochemical reaction rate is determined by current density, the dynamics of how ions move in the electrolyte is complicated by factors such as electrolyte formulation, additives, salt concentration, and temperature [13–17]. Due to limitations in the electrolyte's ion transport rate, a concentration gradient forms near the anode surface, known as concentration polarization. When the current density exceeds the limiting current density, the rate of lithium-ion consumption at the anode surface surpasses the ion transport rate. This imbalance leads to a depletion of lithium ions at the anode surface over a prolonged plating period. The depletion intensifies non-uniform lithium ionic flux near the surface, promoting a transition from mossy dendrite growth to fractal dendrite growth [18–20].

The limiting current density, serving as a safety threshold for the plating process, defines the onset current density that triggers the

<sup>\*</sup> Corresponding author.

E-mail addresses: [chchen@iam.ntu.edu.tw](mailto:chchen@iam.ntu.edu.tw) (C.-H. Chen), [kcc@iam.ntu.edu.tw](mailto:kcc@iam.ntu.edu.tw) (K.-C. Chen).

<sup>1</sup> Contributed equally to this work

formation of fractal dendrites. The Sand model is widely used to determine the value of this safety threshold. Consider lithium plating under a given current density  $i$  in an electrochemical cell using a typical electrolyte system with ethylene carbonate (EC) and  $\text{LiPF}_6$ . Let  $L$  represent the inter-electrode distance,  $c_0$  the bulk concentration, and  $D^+$  and  $D^-$  denote the diffusivities of cations and anions, respectively. The limiting current density, according to the Sand model, is given by [12,20,21]:

$$i_{lim}^* = \frac{2z^+c_0DF}{(1-t^+)L}, \quad (1)$$

where  $F$  denotes the Faraday constant,  $z^+$  is the charge number of the cation (in this study,  $z^+ = 1$  for lithium ions), and  $D = 2D^+D^-/(D^+ + D^-)$  represents the apparent diffusivity of the electrolyte [9,14,20]. The transference number  $t^+ = D^+/(D^+ + D^-)$  number indicates the fraction of lithium ions contributing to the overall ionic conductivity in the electrolyte [22,23].

However, Sand's derivation relies on the assumption of a constant diffusion coefficient in electrolytes. Experiments reveal discrepancies in the onset of lithium dendrite formation between analytical predictions and experiments [9,24–26]. The inconsistency could be attributed to the complex ion transport dynamics in realistic scenarios, influenced by factors like electrolyte composition, solvation structure, ion interactions, lithium salt concentration, and temperature [13–17].

For instance, it is generally observed that ion diffusivity decreases with the salt concentration, primarily due to high viscosity in concentrated solutions. Stewart and Newman propose a diffusivity model for describing this relationship, as given by [15–17].

$$D(c) = D_0 e^{-\beta c}, \quad (2)$$

where  $c$  represents the salt concentration,  $D_0$  represents diffusivity at the infinite dilution limit, and  $\beta$  is the exponential fitting parameter controlling the dependency strength. The dependency strength factor  $\beta$  could be influenced by factors such as electrolyte formulation and temperature. Determining the factor  $\beta$  is commonly achieved through experiments and molecular dynamics. As tabulated in Table A.1, the observed values for  $\beta$  can be as high as  $\beta = 2.86 \text{ M}^{-1}$  [16,17,27]. In a plating system with bulk concentration  $c_0 = 1 \text{ M}$  and a high dependency factor,  $\beta = 2.86 \text{ M}^{-1}$ , the diffusivity varies from its bulk value,  $D_0 e^{-2.86} \approx 0.057 D_0$ , to the infinitely dilute value,  $D_0$ , under the condition of ion depletion at the anode surface. This results in a more than 17-fold variation in ion diffusivity across the electrolyte. Therefore, caution should be exercised when imposing the constant diffusivity assumption in the classical Sand's prediction of limiting current density.

Based on the discussion above, we understand that the simplistic diffusivity model in Sand's formula may inadequately capture the complexities in ion transport dynamics, causing discrepancies between predictions and experiments. To reconcile the inconsistency, we present here a phase-field method for modeling lithium plating with a more accurate representation of ion transport complexity in electrolyte. The phase-field model integrates the Stewart-Newman model for capturing the concentration dependency in diffusivity and the Butler-Volmer equation for electrochemical kinetics at the anode-electrolyte interface. One-dimensional analysis is performed to obtain analytical solutions for the concentration distribution in the electrolyte under the steady-state condition, which yield the limiting current density. These analytical results serve as benchmarks for verifying the phase-field model. Using the phase-field model, we explore concentration polarization, the limiting current density, plating stability, and the resulting lithium morphology during plating. Factors such as current density and the concentration dependency in diffusivity are considered in this study. Results from this study are expected to improve our comprehension and predictive precision in phenomena such as concentration polarization, plating instability, and lithium dendrite growth observed in experiments.

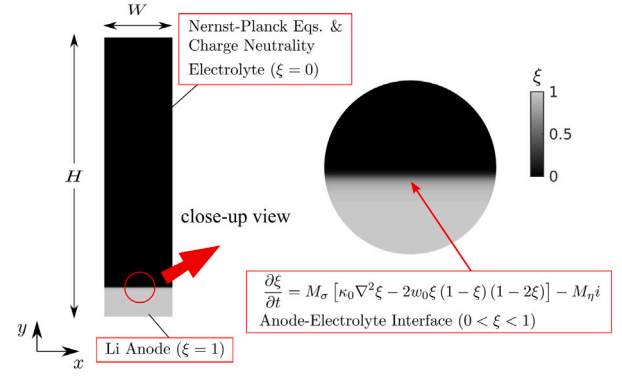


Fig. 1. (Not to scale) Schematic of the phase-field modeling for lithium dendrite formation in a two-dimensional half-cell system of height  $H$  and width  $W$ . The solid lithium anode ( $\xi = 1$ ) is at the bottom, and the liquid electrolyte ( $\xi = 0$ ) fills the space above the anode.  $x$  and  $y$  represent the directions of the width and height of the system, respectively. The interface migration follows the phase-field equation, and ion concentrations adhere to the Nernst-Planck equations under charge neutrality. The initial concentration is  $c_0$ . The system is connected to an imaginary ion reservoir, sustaining a constant concentration of  $c_0$  at  $y = H$  during plating.

## 2. Methodology

### 2.1. Phase-field method

The investigation focuses on lithium plating in a half-cell electrochemical system, illustrated in Fig. 1. The simulation domain is a rectangular box with a height  $H$  and width  $W$  containing a lithium anode at the bottom and an electrolyte filling the remaining space above the anode. Let  $x$  and  $y$  refer to the directions corresponding to the width and height of the system, and  $c_0$  denote the initial lithium ionic concentration in the electrolyte. The application of plating current density  $i$  at the top of the system ( $y = H$ ) drives the conversion of lithium ions to lithium metal at the anode-electrolyte interface.

The phase-field technique is adopted to simulate the evolution of the anode-electrolyte interface during plating, owing to its adaptability in overcoming the numerical complexities associated with tracking the lithium dendrite surface. Originating from the concept of finite-thickness diffusion interfaces introduced by Cahn and Hilliard [28], the phase-field model introduces a scalar variable,  $\xi$ , to differentiate between the liquid electrolyte phase ( $\xi = 0$ ) and the solid anode phase ( $\xi = 1$ ) within an electroplating system. These phases are separated by an interfacial region of thickness  $\delta$ , and the phase variable  $\xi$  varies smoothly across the interface.

Over the past decades, the phase-field method has demonstrated success in electrochemical depositions and lithium dendrite formation [23,29–41]. The adaptability of the phase-field method in accommodating complex morphology evolution and integrating with different physical processes makes it applicable in various areas, not limited to electroplating systems. Examples include microstructural evolution in materials [42,43], dynamic crack propagation [44–50], and viscosity instability [51–53].

The total free energy of an electroplating system in the phase-field model is given by [23,31,32,54]:

$$F = \int \left[ \frac{k_0}{2} |\nabla \xi|^2 + w_0 \xi^2 (1 - \xi)^2 + f_v^{elec} \right] dV. \quad (3)$$

The first term on the right-hand side,  $k_0 |\nabla \xi|^2 / 2$ , accounts for the energy penalty that discourages abrupt changes in the phase interface. The second term,  $w_0 \xi^2 (1 - \xi)^2$ , represents the Ginzburg-Landau double-well potential, capturing the energy contribution associated with the transition of the scalar variable  $\xi$  between its two stable equilibrium states,  $\xi = 0$  and  $\xi = 1$ . The third term,  $f_v^{elec}$ , represents the change in

energy density caused by the phase transformation during electrochemical plating. The coefficients of gradient energy  $k_0$  and the height of the double-well potential  $w_0$  are related to the interfacial thickness  $\delta$  and lithium surface energy  $\gamma$  through the relations  $k_0 = 6\gamma\delta$  and  $w_0 = 3\gamma/\delta$ , respectively [23,29,34,55].

The driving force for anode surface migration during lithium plating is determined by the variational derivative of the total energy  $F$  with respect to the phase variable  $\xi$  as the system evolves towards minimizing the free energy. The phase-field equation, describing the evolution of the phase variable, is given by [23,29,31,32]:

$$\frac{\partial \xi}{\partial t} = M_\sigma \left[ \kappa_0 \nabla^2 \xi - 2w_0 \xi (1 - \xi) (1 - 2\xi) \right] - M_\eta i_{BV}. \quad (4)$$

The rate constant  $M_\eta = \Omega / (6\delta F)$ , and the interfacial mobility  $M_\sigma = i_0 \Omega M_\eta / (RT)$  [23,55,56].  $\Omega$  is the molar volume of the lithium atom,  $i_0$  is the exchange current density,  $R$  is the gas constant,  $F$  is the Faraday constant, and  $T$  is the absolute temperature. The current density at the anode-electrolyte interface follows the Butler-Volmer kinetics [23,31,32]:

$$i_{BV} = h'(\xi) i_0 \left[ e^{(1-\alpha)\eta/\phi_T} - \frac{c^+}{c_0} e^{-\alpha\eta/\phi_T} \right], \quad (5)$$

where  $\eta$  represents the overpotential and  $\alpha$  is the charge-transfer coefficient. Thermal voltage  $\phi_T = RT/F$  provides a characteristic scale for measuring the deviation from the equilibrium potential. The concentration of lithium ions and its initial value are denoted by  $c^+$  and  $c_0$ , respectively. The interpolation function  $h(\xi) = \xi^3 (6\xi^2 - 15\xi + 10)$  represents the fraction of active material participating in the phase transformation during plating. The derivative of the interpolation function,  $h'(\xi) = 30\xi^2 (\xi - 1)^2$  is non-zero within the range of  $0 < \xi < 1$ , and thus the plating only takes place at the anode-electrolyte interface, as described by the Butler-Volmer kinetics in Eq. (5).

Denote  $\phi$  as the electric potential in the electrolyte and  $\phi_a$  as the electric potential in the anode. The electric potential difference at the anode-electrolyte interface is  $\Delta\phi = \phi_a - \phi$ , and the potential difference at equilibrium (i.e., zero net reaction rate) is  $\Delta\phi_{eq}$ . The overpotential in Eq. (5) is the deviation of the electric potential difference from its equilibrium value, expressed as  $\eta = \Delta\phi - \Delta\phi_{eq}$ . Due to the perfect conductivity of lithium metal, and the anode maintains a constant electric potential, this study sets the zero-reference potential at the lithium anode, i.e.,  $\phi_{anode} = 0$ . Additionally, for simplification without loss of generality, the electric potential difference at the equilibrium interface is set to zero ( $\Delta\phi_{eq} = 0$ ), making the overpotential  $\eta = -\phi$  [23,29,31,32].

The Nernst-Planck equations in the phase-field model are modified to include diffusion, electromigration, and lithium-ion reduction at the anode-electrolyte interface, expressed as follows [29,31,54]:

$$\frac{\partial c^+}{\partial t} = \nabla \cdot \left( \overbrace{D^+ \nabla c^+}^{\text{diffusion}} + \overbrace{\frac{D^+ c^+}{\phi_T} \nabla \phi}^{E\text{-migr.}} \right) - \overbrace{c_{Li} \frac{\partial \xi}{\partial t}}^{\text{reduction}}, \quad (6)$$

$$\frac{\partial c^-}{\partial t} = \nabla \cdot \left( D^- \nabla c^- - \frac{D^- c^-}{\phi_T} \nabla \phi \right). \quad (7)$$

Here,  $D^+$  and  $D^-$  represent the diffusivity of cations and anions, respectively. The molar concentration of lithium atoms in the anode is  $c_{Li} = \Omega^{-1}$ . During lithium plating, the binary electrolyte maintains the charge neutrality condition, as given by [54,57–59]:

$$c^+ = c^- = c. \quad (8)$$

Thus, the concentrations of cations  $c^+$ , the concentration of anions  $c^-$ , and the electric potential  $\phi$  are determined using Eq. (6), Eq. (7), and Eq. (8).

The diffusivity of ions in the phase-field model depends on the phase variable  $\xi$  and the concentration  $c$ . We consider that the diffusivity

linearly varies between the solid phase diffusivity  $D_s$  and the liquid phase diffusivity  $D$ , as expressed below:

$$D^\pm(\xi, c) = h D_s + (1 - h) D^\pm(c). \quad (9)$$

The liquid-phase diffusivity  $D^\pm$  and the concentration are related through the Stewart and Newman model [15,16]:

$$D^\pm(c) = D_0^\pm e^{-\beta^\pm c}, \quad (10)$$

where  $D_0^+$  and  $D_0^-$  represent the cation and anion diffusivity at the infinite dilution limit, respectively, and  $\beta^+$  and  $\beta^-$  represent the corresponding concentration dependency values [15]. The literature, summarized in Table A.1, suggests a relatively minor difference between  $\beta^+$  and  $\beta^-$ , with a normalized difference,  $|\Delta\beta|/\bar{\beta}$ , up to 10%, where  $\Delta\beta \equiv \beta^+ - \beta^-$  and  $\bar{\beta} \equiv (\beta^+ + \beta^-)/2$ . For the sake of simplicity in the following discussion, this study considers equal concentration dependencies ( $\beta^+ = \beta^- = \beta$ ), and thus  $D^\pm(c) = D_0^\pm e^{-\beta c}$ .

The numerical parameters utilized in simulations are discussed below. The concentration field is simulated near the anode surface within the Nernst diffusion boundary layer so that the ion transport is governed by the Nernst-Planck equations as convection is negligible. While the system width  $W = 15 \mu\text{m}$  is chosen large enough to accommodate a well-developed structure of lithium dendrites, the selection of a system height  $H = 100 \mu\text{m}$  agrees with the thickness of the diffusion layer in the literature [17,60–62]. The physical constants, including the gas constant  $R = 8.31 \text{ J/(mol K)}$ , the Faraday constant  $F = 9.65 \times 10^4 \text{ C/mol}$ , and the temperature  $T = 300 \text{ K}$ , result in a thermal voltage of  $\phi_T = 26 \text{ mV}$ . The lithium surface energy is  $\gamma = 1.72 \text{ J/m}^2$  [23,55], the exchange current density is  $i_0 = 28 \text{ A/m}^2$  [23,29,63,64], and the molar volume of lithium atoms is  $\Omega = 13 \text{ cm}^3/\text{mol}$  [63,65,66], resulting in a corresponding concentration of lithium atoms in the anode is  $c_{Li} = \Omega^{-1} = 76.92 \text{ M}$ . We employ a symmetric charge-transfer coefficient,  $\alpha = 0.5$  [23,29,63,67], and choose the interfacial thickness  $\delta = 0.5 \mu\text{m}$  in this study. The diffusivity in electrolytes typically has a value between  $10^{-11} - 10^{-10} \text{ m}^2/\text{s}$  [23,63,67,68]. For simplicity, we chosen  $D_0^+ = D_0^- = 10^{-11} \text{ m}^2/\text{s}$  in this study, resulting in a lithium transference number of  $t^+ = 0.5$  [23,29]. The solid phase diffusivity is  $D_s = 10^{-13} \text{ m}^2/\text{s}$ , three orders of magnitude smaller than  $D_0$  for reflecting the significantly slower migration of lithium ions in the solid [67,69–72]. Table 1 summarizes the simulation parameters used in this work.

Regarding the boundary conditions, the lithium plating process is driven by a constant current density  $i$  imposed atop the system ( $y = H$ ). The initial concentration is  $c_0$ , maintained at  $y = H$  through plating by an imaginary reservoir atop the system. During plating, we set zero ion flux across the bottom boundary ( $y = 0$ ), and enforce the phase-field variable  $\xi = 1$  at the bottom boundary and  $\xi = 0$  at the top boundary. Periodic boundary conditions are imposed at the side walls ( $x = 0$  and  $x = W$ ) for both the phase-field variable  $\xi$  and concentration  $c$ .

The computational code is implemented in the C language using the Compute Unified Device Architecture (CUDA) platform. The model's governing equations are spatially discretized using a second-order finite difference scheme on a uniform grid with a mesh size of  $0.05 \mu\text{m}$ . The time integration employs an explicit Euler time-stepping scheme with a time step of  $\Delta t = 5.3 \times 10^{-5} \text{ s}$ . The simulations in this study were conducted on Nvidia Tesla V100-32 GB GPUs. Each simulation run on a single GPU typically required approximately 36 h of computational time. For detailed discussions on non-dimensionalization and numerical implementations of the phase-field model, readers are referred to our previous studies [23,29].

The examination of interface thickness and mesh size was conducted in our previous study, detailed in the Supplementary Information of [29]. Results indicated that the phase-field simulation outcomes were well-converged with an interface thickness of  $\delta = 0.5 \mu\text{m}$  and a mesh size of  $0.1\delta$ . Previous studies [31,38,54] have also verified that the selection of an interface thickness on the order of microns is able to capture accurately the dynamics of anode-electrolyte migration

**Table 1**  
Parameters in phase-field simulations.

Parameter	Symbol	Value	S.I. unit	Source
System height	$H$	100	$\mu\text{m}$	[17,60–62]
System width	$W$	15	$\mu\text{m}$	Set
Gas constant	$R$	8.31	J/(mol K)	Physical constant
Temperature	$T$	300	K	Set
Faraday constant	$F$	$9.65 \times 10^4$	C/mol	Physical constant
Molar volume of Li atom	$\Omega$	13	$\text{cm}^3/\text{mol}$	[63,65,66]
Concentration of Li atom	$c_{Li} = \Omega^{-1}$	76.92	M	[63,65,66]
Li surface energy	$\gamma$	1.72	J/m <sup>2</sup>	[23,55]
Interfacial thickness	$\delta$	0.5	$\mu\text{m}$	Set
Exchange current density	$i_0$	28	A/m <sup>2</sup>	[23,63]
Charge-transfer coefficient	$\alpha$	0.5	–	[63,67]
Transference number	$t^+$	0.5	–	[23]
Infinitely dilute diffusivity (liquid phase)	$D_0^+$	$10^{-11}$	m <sup>2</sup> /s	[23,63,67,68]
Diffusivity (solid phase)	$D_i$	$10^{-13}$	m <sup>2</sup> /s	[67,69–72].
Plating current density	$i$	3–29	A/m <sup>2</sup>	Set

driven by the plating process. This selection balances the accuracy of the model and the computational efficiency; the thickness chosen here is small enough to ensure a consistent with the results at the sharp-interface limit, the mesh size is sufficiently fine for capturing the details of the interface during evolution and maintain computational feasibility.

In addition, it is noted that the charge neutrality may break down within the double layer, a region near the anode surface with a thickness on the order of the Debye screening length  $\lambda_D$ , typically a few nanometers [54,73,74]. The macroscopic phase-field model presented in this study considers the Butler-Volmer kinetics at the anode-electrolyte interface, and the potential jump across the interface is described by the potential of the solid anode and liquid electrolyte in the model. Recent studies reveal that the impact of space charge within the double layer region on lithium dendrite formation during plating instability is very limited and could be negligible, particularly in the early stages of dendrite development [54,57–59]. Hence, with the interface thickness of  $\delta = 0.5 \mu\text{m}$  used in the model, the detailed effects of the nanometer-sized double-layer structure are not explicitly resolved in the model under the spatial resolution selection; alternatively, supported by the aforementioned studies, the charge-neutrality condition is considered in the model.

## 2.2. Steady-state analysis

In addition to phase-field simulations, we also performed analysis for solving the concentration distribution under steady-state conditions and the limiting current density. The obtained analytical results not only provide insights into the impact of ion transport dynamics on plating stability and resulting lithium morphology but also serve as valuable benchmarks for verifying our phase-field simulations. Below, we briefly present our analytical results, and readers can find detailed derivations in Appendix A.

We consider that the uneven ion concentration distribution across the electrolyte is induced by a planar plating process. Due to translational invariance along the lithium surface ( $x$ ), the Nernst-Planck equations simplify to one dimension with  $y$ -dependence. Here, we focus on how concentration distributes across the liquid electrolyte (i.e.,  $\xi = 0$ ), and thus the reduction term in Eq. (6) contributes as the boundary condition. With the Stewart-Newman diffusivity model  $D^\pm(c) = D_0^\pm e^{-\beta c}$  incorporated in the analysis, the steady-state concentration profile obeys the following equation:

$$c^{ss}(y) = c_0 - \frac{1}{\beta} \ln \left[ 1 + e^{\beta c_0} \frac{i(1-t^+)}{D_0 F} \beta (H-y) \right], \quad (11)$$

where  $D_0 = 2D_0^+ D_0^- / (D_0^+ + D_0^-)$ .

The concentration in Eq. (11) monotonically increases with  $y$ . The steady-state surface concentration, i.e., at the anode surface ( $y = 0$ ),

reads:

$$c_{surf}^{ss} = c_0 - \frac{1}{\beta} \ln \left[ 1 + e^{\beta c_0} \frac{i(1-t^+)}{D_0 F} \beta H \right]. \quad (12)$$

By setting the surface concentration  $c_{surf}^{ss} = 0$  in Eq. (12), we obtain the limiting current density:

$$i_{lim} = \left( \frac{1 - e^{-\beta c_0}}{\beta c_0} \right) i_{lim}^*. \quad (13)$$

Here,  $i_{lim}^*$  represents the Sand's limiting current density. Note that  $H$  represents the height of the electrochemical half-cell and  $L$  in Eq. (1) is the inter-electrode distance. With the established relationship  $L = 2H$ , the Sand's limiting current density in a half-cell system is given by:

$$i_{lim}^* = \frac{c_0 D_0 F}{(1-t^+) H}. \quad (14)$$

## 3. Results and discussion

Our investigation begins with phase-field simulations of lithium plating on a flat anode, in which the concentration dependency factor is systematically varied between  $\beta = 0 - 2 \text{ M}^{-1}$ . Fig. 2 illustrates the time evolution of the concentration distribution in phase-field simulations at current density  $i = 5 \text{ A/m}^2$  for different  $\beta$  values:  $\beta = 0 \text{ M}^{-1}$  in (a),  $\beta = 1 \text{ M}^{-1}$  in (b),  $\beta = 1.5 \text{ M}^{-1}$  in (c), and  $\beta = 2 \text{ M}^{-1}$  in (d). The applied current density  $i = 5 \text{ A/m}^2$  is below the limiting values for all simulations, and thus the plating process follows a reaction-limited mechanism. According to the results in Fig. 2, we observed in simulations that the concentration profiles approach their final ones without undergoing ionic depletion. These final profiles consistently align with the analytical predictions in Eq. (11). Furthermore, we found that the concentration profiles for non-zero  $\beta$  values deviate from Sand's linear prediction, especially at high  $\beta$  values.

To demonstrate the model's ability to capture both the evolution of anode-electrolyte interfacial migration and ion transport dynamics during plating, we illustrate in Fig. 3a the phase variable  $\xi$  and surface concentration  $c_{surf}$  at selected plating times in phase-field simulation with  $\beta = 1.0 \text{ M}^{-1}$  at  $i = 5 \text{ A/m}^2$ . Here, the iso-surface of  $\xi = 0.5$  defines the anode surface, and the surface concentration corresponds to the concentration at this iso-surface. During planar plating, the surface migration velocity  $v$  and the applied current density  $i$  are related via  $v = i\Omega/F$  [31,32,55]. With the chosen current density of  $i = 5 \text{ A/m}^2$ , the surface migration is estimated to be approximately  $v = 6.74 \times 10^{-4} \mu\text{m/s}$ . Based on this, the expected migration distance of the anode surface, on the order of a few microns, within the plating duration of approximately 20 min, agrees with our phase-field simulation results in Fig. 3a.

As illustrated in Fig. 3b, the surface concentration decreases monotonically over time, ultimately approaching its final value  $c_{surf}^f$ . The transient time  $\tau_{trans}$  (black empty squares) represents the time for an



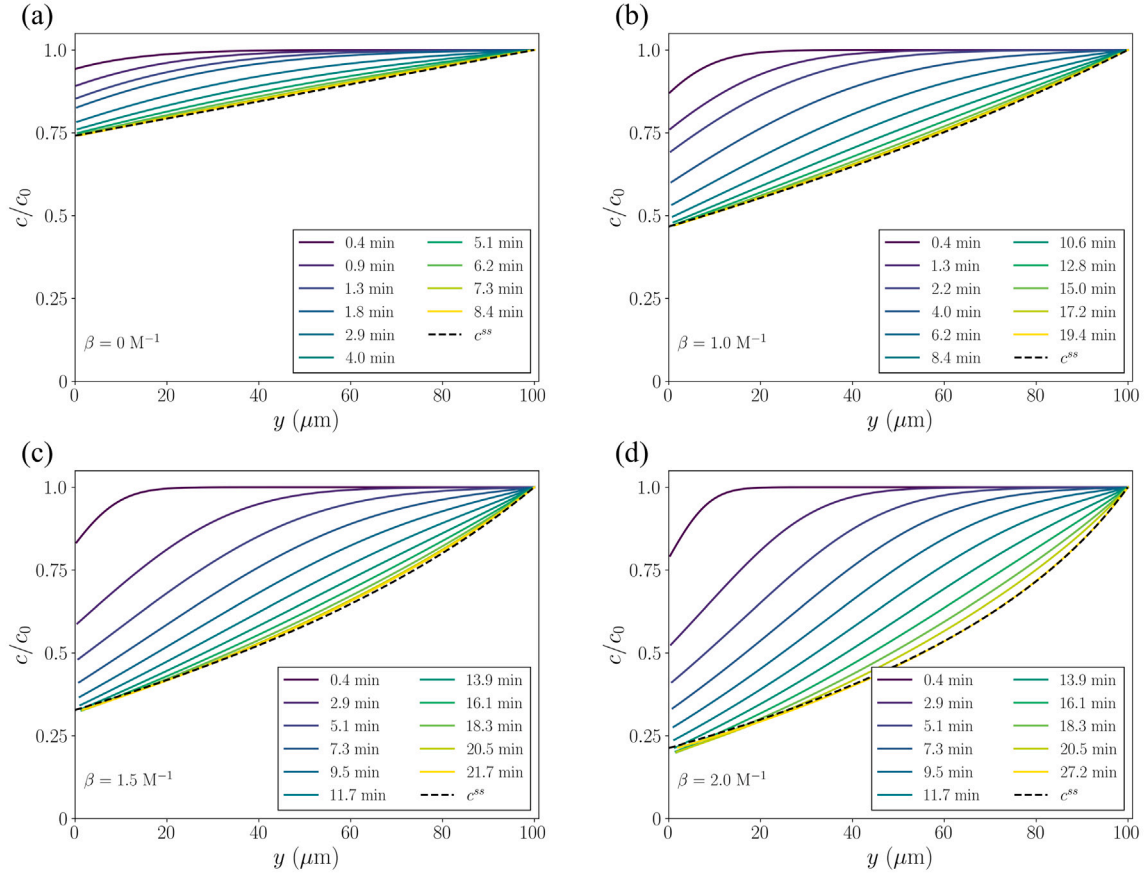


**Fig. 2.** (Color online) Concentration distribution across electrolyte over time for different  $\beta$  values:  $\beta = 0 \text{ M}^{-1}$  (a),  $\beta = 1 \text{ M}^{-1}$  (b),  $\beta = 1.5 \text{ M}^{-1}$  (c), and  $\beta = 2 \text{ M}^{-1}$  (d). Dashed lines illustrate steady-state concentration profiles, showing good agreement with phase-field simulations. Final concentration distributions deviate from Sand's model, especially at high  $\beta$  values.

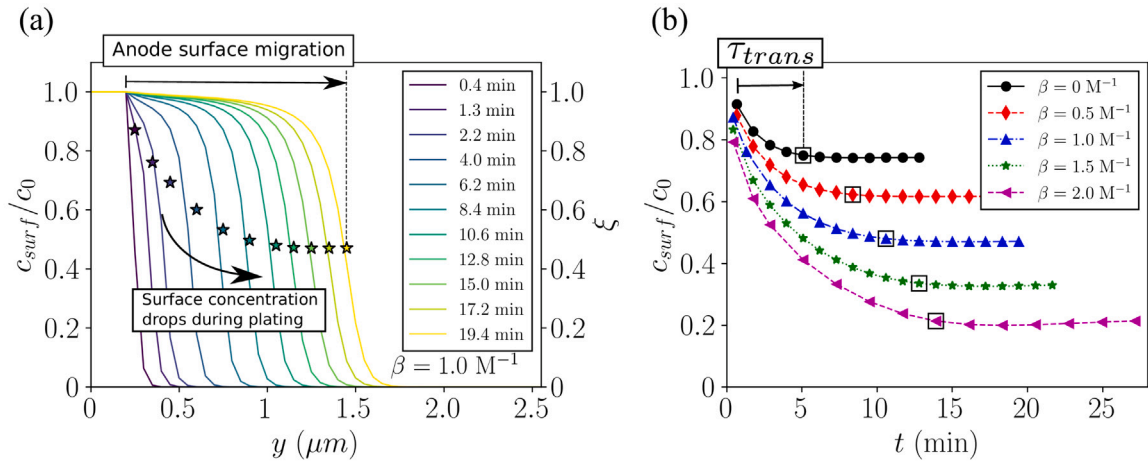


**Fig. 3.** (Color online) (a) Illustration of phase-field model's ability to capture both the evolution of interfacial migration ( $\xi$ , solid lines) and surface concentration ( $c_{surf}$ , asterisks) from simulation with  $\beta = 1.0 \text{ M}^{-1}$  and  $i = 5 \text{ A/m}^2$ . (b) Temporal evolution of surface concentration in phase-field simulations with varying  $\beta$  values. Increasing  $\beta$  results in a lower surface concentration and a prolonged transient time. The observed transient times (empty squares) are  $\tau_{trans} = 5.08 \text{ min}$  for  $\beta = 0 \text{ M}^{-1}$ ,  $\tau_{trans} = 8.40 \text{ min}$  for  $\beta = 0.5 \text{ M}^{-1}$ ,  $\tau_{trans} = 10.60 \text{ min}$  for  $\beta = 1.0 \text{ M}^{-1}$ ,  $\tau_{trans} = 12.81 \text{ min}$  for  $\beta = 1.5 \text{ M}^{-1}$ , and  $\tau_{trans} = 13.92 \text{ min}$  for  $\beta = 2.0 \text{ M}^{-1}$ .

electroplating system to reach its steady-state solutions. It is defined, specifically, in this study as the earliest plating time for the surface concentration reaching the final value  $c_{surf}^f$ , within an insignificant difference of 1%.

The transient times observed in the phase-field simulations are  $\tau_{tran} = 5.08 \text{ min}$  for  $\beta = 0 \text{ M}^{-1}$ ,  $\tau_{tran} = 8.40 \text{ min}$  for  $\beta = 0.5 \text{ M}^{-1}$ ,

$\tau_{tran} = 10.60 \text{ min}$  for  $\beta = 1.0 \text{ M}^{-1}$ ,  $\tau_{tran} = 12.81 \text{ min}$  for  $\beta = 1.5 \text{ M}^{-1}$ , and  $\tau_{tran} = 13.92 \text{ min}$  for  $\beta = 2.0 \text{ M}^{-1}$ . Overall, our phase-field simulation results demonstrate that under a given current density, the increase in  $\beta$  results in a twofold effect: (i) a decrease in the final surface concentration and (ii) a prolonged transient time for a steady state to establish.

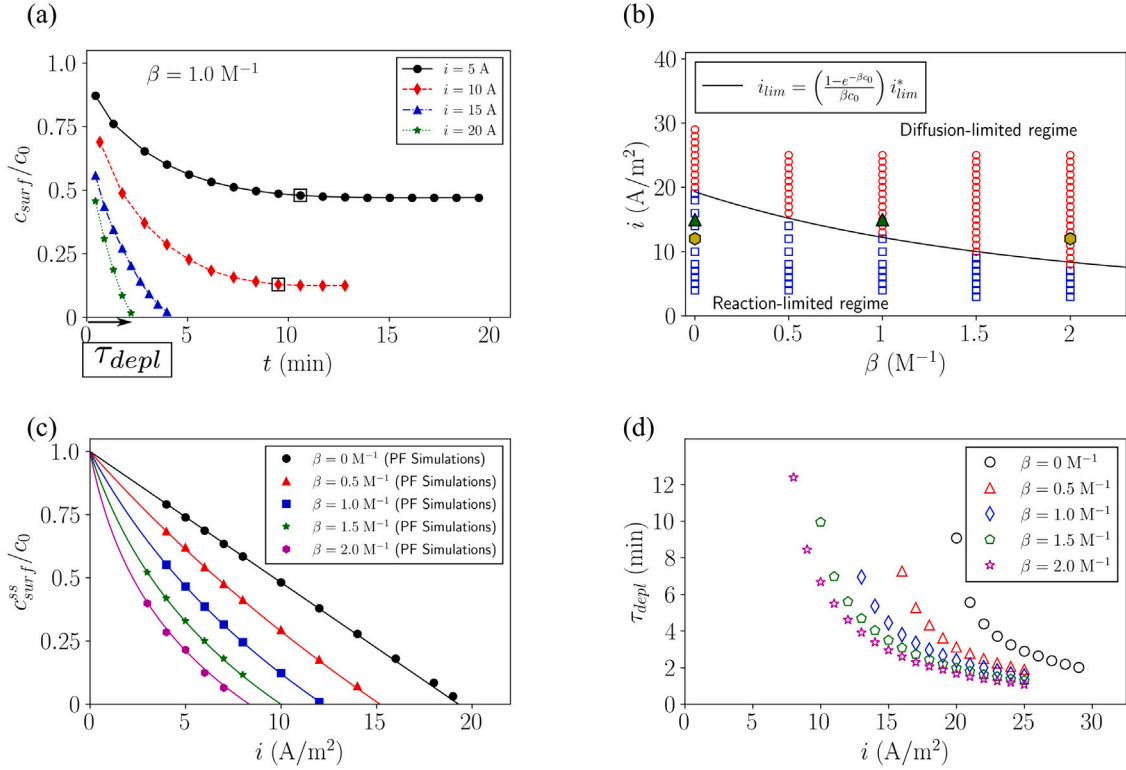


**Fig. 4.** (Color online) (a) Surface concentration ( $c_{surf}$ ) versus time in phase-field simulations for different current densities. In reaction-limited regime ( $i = 5 \text{ A/m}^2$  and  $i = 10 \text{ A/m}^2$ ), surface concentration converges to its steady-state value. In diffusion-limited regime ( $i = 15 \text{ A/m}^2$  and  $i = 20 \text{ A/m}^2$ ), surface concentration depletes within  $\tau_{depl}$ . (b) Phase diagram illustrates two observed plating behaviors, the reaction-limited (blue squares) and diffusion-limited (red circles) regimes, as a function of current density  $i$  and concentration dependency factor  $\beta$ . Analytical steady-state profiles (solid lines) in Eq. (13) align consistently, confirming limiting current density predictions agreement. Green triangles represent the simulations for stable plating ( $\beta = 0 \text{ M}^{-1}$ ) and unstable plating ( $\beta = 1.0 \text{ M}^{-1}$ ) at current density of  $i = 15 \text{ A/m}^2$  in Fig. 5b and Fig. 5c, respectively. Yellow hexagons represent the simulations for mossy dendrites ( $\beta = 0 \text{ M}^{-1}$ ) and fractal dendrites ( $\beta = 2.0 \text{ M}^{-1}$ ) at current density of  $i = 12 \text{ A/m}^2$  in Fig. 6a and Fig. 6b, respectively. (c) Steady-state surface concentration  $c_{surf}^{ss}$  versus current density  $i$  for different  $\beta$  values. Comparison of simulations (markers) and analytical solution by Eq. (12) (lines) reveals good agreement. (d) Depletion time  $\tau_{depl}$  versus current densities for different  $\beta$ , revealing a faster ion depletion at higher current densities and larger  $\beta$  values.

We repeated the phase-field simulations by varying the applied current density between  $i = 3\text{--}29 \text{ A/m}^2$  for different  $\beta$  values, and we monitored the evolution of the surface concentration during plating. Results from an illustrative simulation with  $\beta = 1.0 \text{ M}^{-1}$  in Fig. 4a highlight the distinct behaviors at low and high current density regimes. At low current densities ( $i = 5 \text{ A/m}^2$  and  $i = 10 \text{ A/m}^2$ ), the surface concentration  $c_{surf}$  converges to final steady-state values within their corresponding transient times ( $\tau_{trans} = 10.60 \text{ min}$  and  $\tau_{trans} = 9.50 \text{ min}$ ) without undergoing depletion. The lithium plating is predominantly controlled by reaction kinetics at the interface, and the plating dynamics under this condition is characterized as the reaction-limited regime. In contrast, as plating at high current densities ( $i = 15 \text{ A/m}^2$  and  $i = 20 \text{ A/m}^2$ ), the surface concentration rapidly decreases and depletes for a sufficiently long plating time. The time required for ion depletion, in terms of the depletion time, is denoted by  $\tau_{depl}$ . The lithium plating is controlled by ion transport across the electrolyte, and the plating dynamics under this condition is characterized as the diffusion-limited regime.

The phase diagram (Fig. 4b) categorizes the phase-field observed lithium plating dynamics into reaction-limited regime (blue squares) and diffusion-limited regime (red circles), as a function of the plating current density  $i$  and the concentration dependency factor  $\beta$ . The boundary of the two distinct plating dynamics, reaction-limited and diffusion-limited, agrees well with the analytical prediction of the limiting current density given by Eq. (13). This observation confirms the accuracy of our model in capturing the transition between distinct lithium plating behaviors. Our results in Fig. 4b further suggest a decrease in the limiting current density with increasing  $\beta$ . While Sand's

limiting current density in Eq. (14) yields  $i_{lim}^* = 19.3 \text{ A/m}^2$ , the observed limiting current density deviates from this value, particularly at higher  $\beta$  values.

Fig. 4c illustrates the steady-state surface concentration  $c_{surf}^{ss}$  as a function of current density  $i$  for different  $\beta$  values from reaction-limited plating simulations. We observed that  $c_{surf}^{ss}$  decreases with both the current density  $i$  and the concentration dependency factor  $\beta$ . These phase-field simulated results align well with the predictions by Eq. (12) (solid lines), demonstrating a consistent agreement between phase-field simulations and analytical results. For simulations belonging to the diffusion-limited regime, we examined their depletion behaviors, and the measured depletion time  $\tau_{depl}$  versus current density  $i$  for different  $\beta$  values is plotted in Fig. 4d. Since the ion transport is slower in electrolytes with a high  $\beta$  value, along with the fact that high current density accelerates the depletion of surface ions, the depletion time, as expected, decreases with both current density  $i$  and the concentration dependency factor in diffusivity  $\beta$ .

We conducted additional phase-field simulations to investigate the impact of concentration-dependent diffusion on lithium plating instability and resulting lithium morphology. To examine the stability of anode-electrolyte interfacial migration during plating, a small semicircular lithium with a radius of  $1 \mu\text{m}$  was initially inserted atop the flat anode, as shown in Fig. 5a. Snapshots in Fig. 5b and Fig. 5c depict the evolving lithium morphology at different selected times during plating at a current density of  $i = 15 \text{ A/m}^2$  for  $\beta = 0 \text{ M}^{-1}$  and  $\beta = 1 \text{ M}^{-1}$ , respectively. To better visualize concentration variation near the anode surface effectively, the images are color-coded with

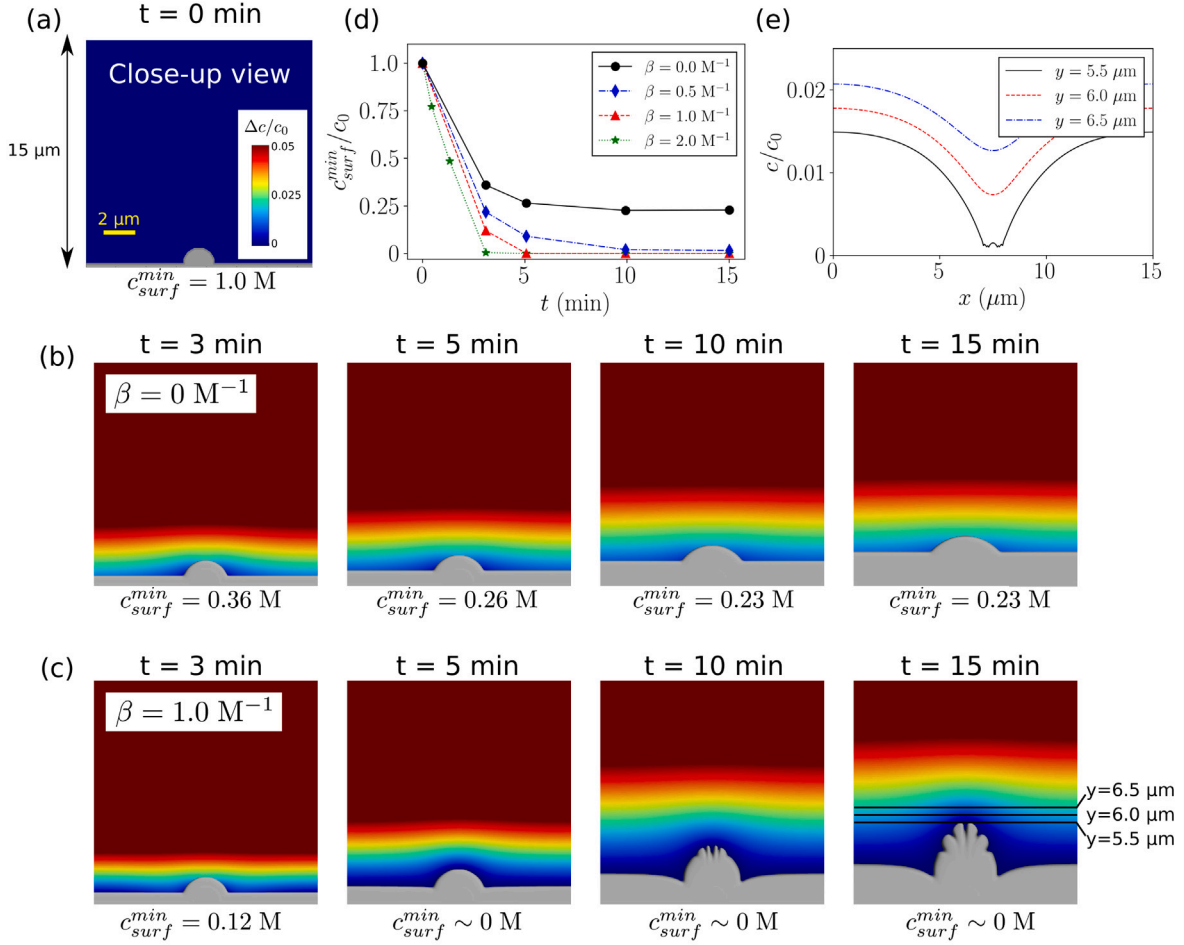


**Fig. 5.** (Color online) Two-dimensional phase-field lithium morphologies at current density  $i = 15 \text{ A/m}^2$ . (a) Close-up view of the initial configuration of lithium anode in simulations of height  $H = 100 \mu\text{m}$  and width  $W = 15 \mu\text{m}$ . Snapshots of lithium morphologies at different plating times for  $\beta = 0 \text{ M}^{-1}$  in (b) and  $\beta = 1.0 \text{ M}^{-1}$  in (c). Colors in (a-c) represent the normalized concentration difference  $\Delta c/c_0$ , where  $\Delta c \equiv c - c_{surf}^{min}$ , and  $c_{surf}^{min}$  is the minimum of the surface concentration. (d) Temporal evolution of  $c_{surf}^{min}$  for different  $\beta$  values shows ion depletion as  $\beta$  exceeds  $0.5 \text{ M}^{-1}$ . Black circles ( $\beta = 0 \text{ M}^{-1}$ ) and red triangles ( $\beta = 1.0 \text{ M}^{-1}$ ) correspond to simulations in (b) and (c), respectively. (e) Concentration profiles at  $y = 5.5 \mu\text{m}$ ,  $6.0 \mu\text{m}$  and  $6.5 \mu\text{m}$  in simulation with  $\beta = 1.0 \text{ M}^{-1}$  at  $t = 15$  min, as indicated in the final snapshot in (c).

normalized concentration differences  $\Delta c/c$ , where  $\Delta c = c - c_{surf}^{min}$ , and  $c_{surf}^{min}$  represents the minimum surface concentration.

As depicted in Fig. 5b, a stable plating process was observed in the simulation with  $\beta = 0 \text{ M}^{-1}$ . The surface concentration decreases over time, reaching a steady-state concentration of  $c_{surf}^{min} = 0.23 \text{ M}$  at  $t = 10$  min. The plating is reaction-limited, and the concentration at the anode surface maintains a relatively stable lithium plating process. On the other hand, in simulation with  $\beta = 1.0 \text{ M}^{-1}$ , the application of the same current density  $i = 15 \text{ A/m}^2$  results in the depletion of ions at the anode surface within  $t = 5$  min, and consequently, we observed the growth of irregular lithium dendrites during a 15-min unstable plating, as illustrated in Fig. 5c. The temporal evolution plots of the minimum surface concentration,  $c_{surf}^{min}$ , in Fig. 5d show that plating is under the reaction-limited regime for  $\beta = 0 \text{ M}^{-1}$  and shifts to the diffusion-limited regime for  $\beta$  exceeding  $0.5 \text{ M}^{-1}$ , where the ion depletion is clearly observed. These results reveal a close correlation between the observed lithium dendrite formation and the surface ion depletion. To illustrate the influence of lithium morphology on surface concentration distribution, we plot in Fig. 5e the concentration profiles at different heights:  $y = 5.5 \mu\text{m}$ ,  $6.0 \mu\text{m}$ , and  $6.5 \mu\text{m}$ . It is evident that the concentration varies considerably spatially, especially at  $y = 5.5 \mu\text{m}$ . The valley region, with nearly vanishing concentration at  $x = 7.5 \mu\text{m}$ , suggests the ion depletion due to the presence of lithium dendrites. As one moves away from the dendrite surface, the concentration increases, with less pronounced variation in the  $x$ -direction as expected. Our results suggest

a clear correlation between spatial concentration variation and lithium dendrite morphology.

The discussion above focuses on investigating the impact of concentration dependency in diffusivity on the limiting current density, above which the plating becomes unstable due to ion depletion and yields diffusion-controlled lithium dendrites. However, lithium plating in reality is rarely stable even below the theoretical limiting current density. For example, lithium whiskers are observed at low current densities, while mossy lithium dendrites are commonly observed under typical charging conditions [9,20]. This development of lithium dendrites at under-limiting current densities is closely linked to a thin passivation layer termed the solid electrolyte interface (SEI), composed of electrolyte decomposition compounds that spontaneously form on the surface of the lithium anode [9,66,75–77]. For these irregular dendrites forming at under-limiting current densities, lithium whiskers pose minimal safety risks due to easy blockage by separators, while mossy dendrites could pose safety concerns due to their ability to penetrate separators [7,9,20].

We then explore the formation of mossy dendrites under the influence of concentration-dependent diffusivity in the phase-field simulations. Lithium plating on significantly curved anode surfaces is non-uniform, which often results in the growth of mossy dendrites, even at under-limiting current densities. This growth is attributed to a tip-preferential plating mechanism that is linked to the inherent inhomogeneity of the SEI [66,78]. The significant volume changes

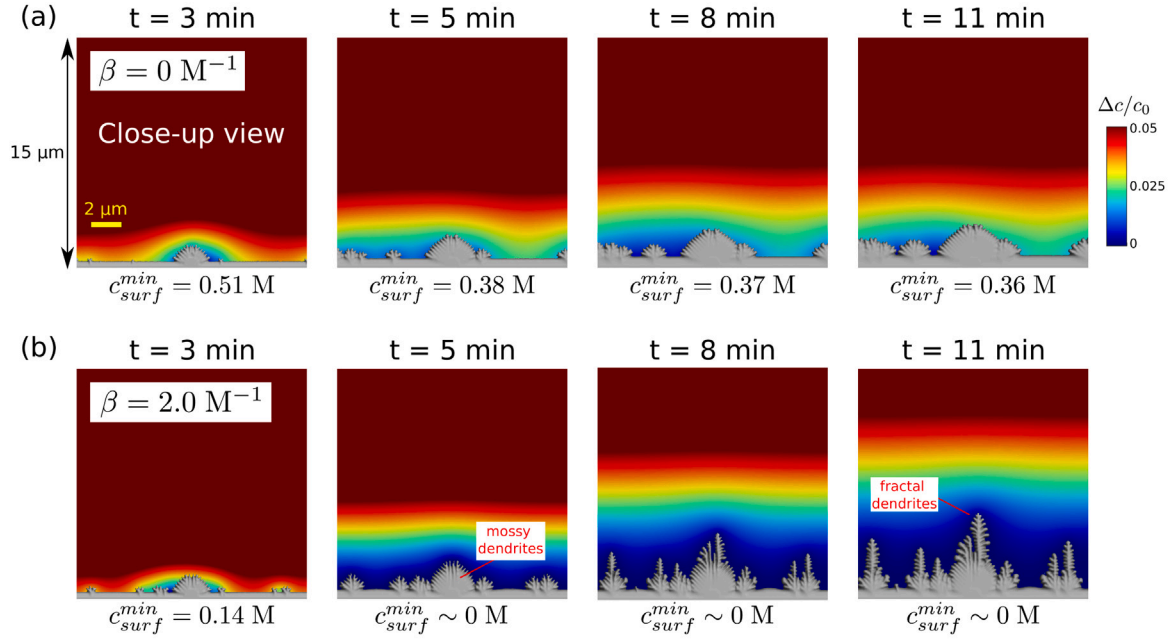


**Fig. 6.** (Color online) Close-up views of lithium morphologies at current density  $i = 12 \text{ A/m}^2$  with the incorporation of the tip-preferential plating mechanism through a rate modification factor  $S$  in phase-field simulations of height  $H = 100 \text{ }\mu\text{m}$  and width  $W = 15 \text{ }\mu\text{m}$ . (a) In the case of  $\beta = 0 \text{ M}^{-1}$ , tip-preferential plating, characterized by fast plating rates at dendrite tips and slower rates on the surface away from the tips, leads to mossy dendrite growth. (b) With high concentration dependency in diffusivity ( $\beta = 2.0 \text{ M}^{-1}$ ), ion depletes under the same current density, triggering a transition from mossy to fractal dendrites. Colors represent the normalized concentration difference  $\Delta c/c_0$ , where  $\Delta c \equiv c - c_{surf}^{min}$ , and  $c_{surf}^{min}$  is the minimum of the surface concentration.

during plating can induce stress in highly deformed areas, particularly those with high curvature. This stress can lead to the disintegration of the SEI structure once it exceeds a critical threshold ( $\sigma > \sigma_c$ ), resulting in incomplete SEI coverage on the anode surface [9,23,29].

The SEI is composed of solid compounds from the decomposition of the electrolyte. It shows slow ion transport compared to liquid electrolytes. When the SEI is damaged, cracks within it are filled with electrolyte solutions, which allows for fast ion migration. Our recent research proposes a two-pathway model, suggesting that fast ion migration occurs at fractured SEI while slow migration occurs at intact SEI. This model successfully explains the mechanism of tip-preference deposition, the key to the formation of commonly observed mossy lithium dendrites below the limiting current density [23,29].

In order to incorporate the tip-deposition mechanism into the phase-field model, we introduce a rate modification factor  $S$  to regulate the electrochemical kinetics at the interface in an ad-hoc manner. Here,  $S$  represents a rate modification factor that accounts for the variation in kinetics from slow kinetics with  $S_{slow}$  at the intact SEI ( $\sigma < \sigma_c$ ) to fast kinetics with  $S_{fast}$  at the fractured SEI ( $\sigma > \sigma_c$ ) [23,29]. The electrochemical kinetics follows a modified Butler-Volmer equation given by  $i_{BV}^{modified} = Si_{BV}$ , and then the phase-field equation in Eq. (4) becomes:

$$\frac{\partial \xi}{\partial t} = M_\sigma [\kappa_0 \nabla^2 \xi - 2w_0 \xi (1 - \xi)(1 - 2\xi)] - M_\eta Si_{BV}. \quad (15)$$

The stress  $\sigma$  and local curvature  $\kappa$  are related through Stoney's equation:  $\kappa = [6(1 - \nu_a)h_{sei}/(E_a h_a^2)]\sigma$ , where  $E_a$ ,  $\nu_a$ , and  $h_a$  denote the Young's modulus, Poisson's ratio, and anode's thickness, respectively, and  $h_{sei}$  represents the thickness of the SEI [79–81]. The three essential parameters used in simulations of Fig. 6 are  $S_{fast} = 1$ ,  $S_{slow} = 0.1$ , and the critical curvature for SEI rupture  $\kappa_c = 2.0 \text{ }\mu\text{m}^{-1}$ . Further details about the parameter settings and model description can be found in [23,29].

Close-up views in Fig. 6 illustrate the evolution of lithium morphology at different selected times during plating at current density  $i = 12 \text{ A/m}^2$  for  $\beta = 0 \text{ M}^{-1}$  and  $\beta = 2.0 \text{ M}^{-1}$ . According to our simulation results in Fig. 6a (see also Movie S1), in the case of  $\beta = 0 \text{ M}^{-1}$ , we

found that the inhomogeneity in lithium deposition, characterized by fast plating rates at the tips of lithium dendrites and slower rates on the surface away from the tips, leads to the mossy dendrite growth with a surface concentration approaching to its final value  $c_{surf}^{min} \sim 0.36 \text{ M}$  at  $t = 11 \text{ min}$ . With a high concentration-dependency in diffusivity ( $\beta = 2.0 \text{ M}^{-1}$ ), we observed the development of mossy dendrites at the early stage of plating, followed by the formation of fractal dendrites. The depletion of ions at  $t = 5 \text{ min}$  triggers the transition in lithium dendrite growth from mossy dendrites to fractal dendrites, as shown in Fig. 6b (see also Movie S2). These results not only demonstrate our model's ability to simulate realistic, complex lithium morphology during plating instability under the influence of concentration-dependency in diffusivity, but also reveal the substantial impact of the concentration-dependency in diffusivity on different lithium dendrite growth mechanisms.

#### 4. Conclusion

Electroplating induces concentration polarization. Once the plating current density surpasses a safety threshold, termed the limiting current density, ion depletion occurs, and the fractal dendrites develop. The Sand's model is used widely for limiting current density predictions. However, overlooking concentration's influence on ion transport dynamics leads to discrepancies between predictions and experimental observations. To better comprehend the impact of concentration-influenced diffusivity on plating stability and the resulting lithium morphology, we conducted numerical investigations in this work, including phase-field simulations and steady-state analysis. The phase-field model integrates the Butler-Volmer equation to describe reaction kinetics at the anode-electrolyte interface and Stewart-Newman's diffusivity to account for the decreasing diffusivity at high concentrations.

First, we explored the concentration polarization during planar plating in simulations, where the phase-field model captures the evolution of the concentration distribution across the electrolyte during anode-electrolyte interfacial migration. Our simulation results reveal two distinct plating behaviors, separated by the limiting current density. In the



under-limiting regime (plating current density below the limit), surface concentration approaches final values under steady-state conditions. The observed concentration profiles deviate from Sand's model predictions, with inconsistency becoming pronounced at larger  $\beta$  values, where  $\beta$  is the exponentially fitting parameter in Stewart-Newman's model controlling the concentration dependency in diffusivity. On the other hand, we observed surface concentration in the over-limiting regime (plating current density above the limit) dropping to zero within a finite depletion time. This ion depletion is identified as a crucial factor that triggers the plating instability and the consequent formation of lithium dendrites.

Additionally, we performed a one-dimensional analysis to examine the impact of concentration-dependent diffusivity on lithium plating. Our analysis shows that in the reaction-limited regime, the concentration profiles in the Stewart-Newman model with non-zero  $\beta$  values follow a logarithmic distribution along the plating direction in the electrolyte, deviating from the classical Sand's linear distribution. In comparing our analytical predictions, which involve the concentration distributions and the limiting current density, with the simulation results conducted under steady-state conditions, we demonstrate a good agreement between phase-field simulations and analysis.

Finally, our two-dimensional phase-field study reveals that the concentration dependency in diffusivity can significantly influence the lithium plating stability and dendrite morphology. In the case of  $\beta = 0$ , reflecting a constant diffusivity assumption in Sand's model, our observations indicate that the concentration reaches a steady-state solution without depletion, yielding a relatively stable lithium growth. In contrast, lithium plating becomes unstable in simulations with non-zero  $\beta$ , resulting in ion depletion and the growth of diffusion-controlled lithium dendrites for sufficient plating time. By incorporating inherent non-uniform plating linked to the nature of SEI inhomogeneity into the phase-field model, our results show the proposed phase-field model's capability to capture realistic, complex mossy dendrite growth dynamics under the influence of the concentration-dependent diffusivity, and reveal a transition from reaction-limited mossy dendrites to diffusion-limited fractal dendrites as ion depletes in simulations with a high concentration-dependency in diffusivity. Overall, this work provides insights into concentration-influenced ion transport dynamics on plating stability, addressing discrepancies in limiting current density between experimental data and Sand's predictions.

The dynamics of ion transport can vary significantly between conventional and highly concentrated electrolytes. Conventional electrolytes typically follow a vehicle-type mechanism, whereas experiments suggest that highly concentrated electrolytes with coordinating solvents form a solvent-bridged network, which facilitates hopping transport. This mechanism reduces concentration polarization, increases current density, and mitigates lithium dendrite formation [82, 83]. Therefore, it is important to exercise caution when extending these findings to such electrolytes, as the Stewart-Newman diffusivity may become irrelevant. We below outline promising extensions of this study. The present work examines the case of  $t^+ = 0.5$ . The lithium transference number exhibits considerable variation based on the specific electrolyte formulation. Exploring its impact on plating dynamics is worthwhile by varying the transference number within the observed range. In addition, it is valuable to extend the current analysis beyond steady-state conditions to explore the transient dynamics of ion transport behaviors in the electrolyte, solving analytically for the depletion time. While this study investigated the influence of ion diffusivity in the electrolyte on lithium plating, as suggested by recent research [25,29,84,85], the transport of ions across the anode-electrolyte interface also plays a crucial role in the formation of lithium dendrites. Thus, future improvements to the present phase-field model should involve investigating the influence of the SEI's diffusivity for a comprehensive understanding.

## CRediT authorship contribution statement

**Chi-Jyun Ko:** Writing – review & editing, Writing – original draft, Validation, Software, Investigation, Formal analysis. **Chen-Ning Tai:** Writing – review & editing, Writing – original draft, Validation, Software, Investigation, Formal analysis. **Chih-Hung Chen:** Writing – review & editing, Writing – original draft, Supervision, Funding acquisition, Conceptualization. **Kuo-Ching Chen:** Writing – review & editing, Writing – original draft, Supervision, Funding acquisition, Conceptualization.

## Declaration of competing interest

The authors declare that they have no known competing financial interests or personal relationships that could have appeared to influence the work reported in this paper.

## Data availability

Data will be made available on request.

## Acknowledgments

This work was supported by the National Science and Technology Council of Taiwan under Grant NSTC-111-2222-E-002-011-MY2. The authors are grateful to Computer and Information Networking Center, National Taiwan University for the support of high-performance computing facilities.

## Appendix A. Steady-state analysis

We present a one-dimensional analysis for solving the concentration distribution under steady-state conditions and the limiting current density. The analysis builds upon Akolkar's foundational work in developing a mathematical framework for dendritic growth during electrodeposition [17,60]. As depicted in Fig. A.1, the uneven distribution of ion concentration across the electrolyte is caused by the planar plating process. Due to the system's translational invariance along the lithium surface ( $x$ -direction), the governing Nernst–Planck equations simplify to a one-dimensional expression with only  $y$ -dependence. In the steady-state analysis, we pay attention to the concentration in the electrolyte (i.e.,  $\xi = 0$ ), with the reduction term in Eq. (6) serving as a boundary condition.

As the steady-state condition is established, i.e.,  $\partial c^\pm / \partial t = 0$ , we employ the charge neutrality condition  $c^+ = c^- = c$  to rewrite the governing equations for  $c^+$  and  $c^-$  given in Eqs. (6) and (7):

$$\frac{\partial}{\partial y} \left( D^+ \left[ \frac{\partial c}{\partial y} + c \frac{\partial (\phi / \Phi_T)}{\partial y} \right] \right) = 0 \quad (\text{A.1})$$

$$\frac{\partial}{\partial y} \left( D^- \left[ \frac{\partial c}{\partial y} - c \frac{\partial (\phi / \Phi_T)}{\partial y} \right] \right) = 0 \quad (\text{A.2})$$

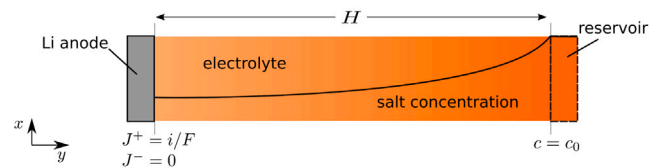


**Fig. A.1.** Schematics of lithium-ion concentration distribution in the electrolyte during a planar plating process in our steady-state analysis.  $x$  and  $y$  represent the directions corresponding to the width and height of the system, respectively. The system is connected to an imaginary ion reservoir, maintaining a constant concentration  $c_0$  at  $y = H$  during plating.

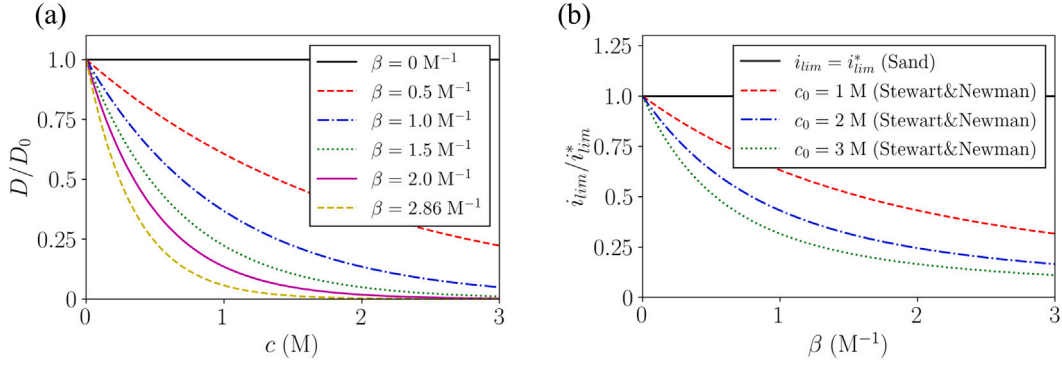


Fig. A.2. (a) Plots of the Stewart-Newman diffusivity expressed as  $D = D_0 e^{-\beta c}$  versus concentration  $c$  for various  $\beta$ . (b) Plots of normalized limiting current density  $i_{lim}/i_{lim}^*$  versus  $\beta$  for different bulk concentration  $c_0$ , indicating a noticeable deviation from the Sand's limiting current density  $i_{lim}^*$ .

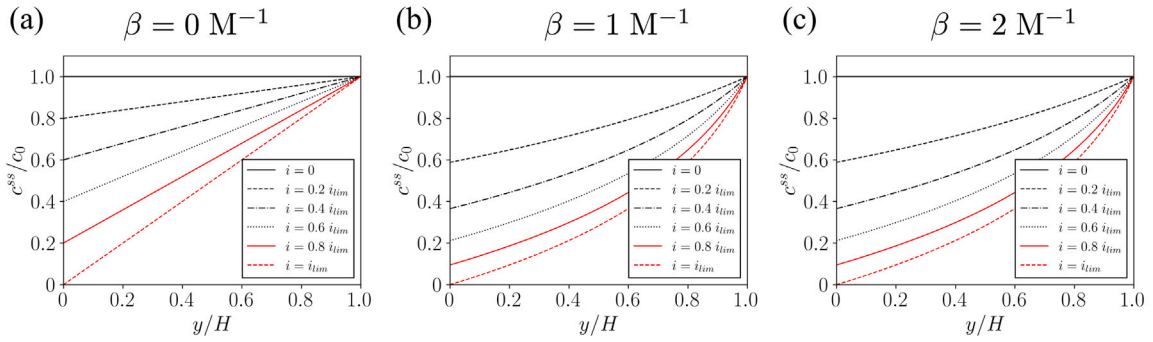


Fig. A.3. Steady-state concentration profiles versus normalized plating current density  $i/i_{lim}$  for different  $\beta$  values: (a)  $\beta = 0 \text{ M}^{-1}$ , (b)  $\beta = 1 \text{ M}^{-1}$  and (c)  $\beta = 2 \text{ M}^{-1}$ . Concentration polarization becomes pronounced at larger current densities. Ion depletion occurs at  $i = i_{lim}$ . Concentration is linearly distributed in  $\beta = 0$ , and follows a logarithmic distribution for non-zero  $\beta$  values, as given in Eq. (A.9).

The utilization of the Stewart-Newman diffusivity model  $D^\pm(c) = D_0^\pm e^{-\beta c}$ , the governing equations are rewritten as:

$$\frac{\partial}{\partial y} \left( D_0^+ e^{-\beta c} \left[ \frac{\partial c}{\partial y} + c \frac{\partial (\phi/\Phi_T)}{\partial y} \right] \right) = 0 \quad (\text{A.3})$$

$$\frac{\partial}{\partial y} \left( D_0^- e^{-\beta c} \left[ \frac{\partial c}{\partial y} - c \frac{\partial (\phi/\Phi_T)}{\partial y} \right] \right) = 0 \quad (\text{A.4})$$

By summing the product of  $D_0^-$  with Eq. (A.3) and the product of  $D_0^+$  with Eq. (A.4), we eliminate the  $\phi$ -dependent terms to obtain:

$$\frac{\partial}{\partial y} \left( e^{-\beta c} \frac{\partial c}{\partial y} \right) = 0 \quad (\text{A.5})$$

The current flow at the anode's surface ( $y = 0$ ) accounts for the reduction of lithium ions, and the prohibition of anions from passing through the electrode's surface results in a vanishing anion flux at the anode surface. These conditions establish the relationship between the current density  $i$  and the flux of cations and anions through the interface, as expressed below:

$$J^+ = D^+ \left[ \frac{\partial c}{\partial y} + c \frac{\partial (\phi/\Phi_T)}{\partial y} \right] \Big|_{y=0} = i/F \quad (\text{A.6})$$

$$J^- = D^- \left[ \frac{\partial c}{\partial y} - c \frac{\partial (\phi/\Phi_T)}{\partial y} \right] \Big|_{y=0} = 0. \quad (\text{A.7})$$

The initial concentration is denoted by  $c_0$ . The system connects to an imaginary reservoir at  $y = H$ , maintaining a constant concentration of  $c_0$  throughout the plating process, and we have:

$$c|_{y=H} = c_0. \quad (\text{A.8})$$

The application of the boundary conditions specified in Eq. (A.6), Eq. (A.7), and Eq. (A.8) into Eq. (A.5) allows to derive the steady-state concentration profile:

$$c(y) = c_0 - \frac{1}{\beta} \ln \left[ 1 + e^{\beta c_0} \frac{i(1-t^+)}{D_0 F} \beta (H-y) \right], \quad (\text{A.9})$$

where  $D_0 = 2D_0^- D_0^+ / (D_0^+ + D_0^-)$ .

The concentration profile in Eq. (A.9) exhibits a monotonic increase with  $y$ , and the concentration at the anode surface  $c_{surf}$  is given by:

$$c_{surf} = c_0 - \frac{1}{\beta} \ln \left[ 1 + e^{\beta c_0} \frac{i(1-t^+)}{D_0 F} \beta H \right] \quad (\text{A.10})$$

Setting the surface concentration  $c_{surf} = 0$  in Eq. (A.10), we obtain the limiting current density:

$$i_{lim} = \left( \frac{1 - e^{-\beta c_0}}{\beta c_0} \right) i_{lim}^*. \quad (\text{A.11})$$

In the special case of  $\beta = 0$ , where diffusivity is independent of concentration ( $D = D_0$ ), the concentration profile in Eq. (A.9) simplifies to:

$$c(y) = c_0 \left[ 1 - i \left( \frac{1-t^+}{c_0 D_0 F} \right) (H-y) \right]. \quad (\text{A.12})$$

The concentration profile in this expression exhibits a linear scaling with respect to  $y$ . Consequently, the limiting current density in Eq. (A.11) reduces to Sand's limiting current density,  $i_{lim}^*$  [12,23,86].

As mentioned in the main text, the exponential fitting parameter  $\beta$  in the Stewart-Newman model controls the concentration dependency in ion diffusivity. Factors like electrolyte formulation and temperature

Table A.1

Concentration-related fitting coefficients,  $D_0$  and  $\beta$ , in Stewart and Newman's diffusivity model as reported in the literature.

Li Salt	$D_0^+$ ( $10^{-10}$ m/s <sup>2</sup> )	$\beta^+$ (M <sup>-1</sup> )	$D_0^-$ ( $10^{-10}$ m/s <sup>2</sup> )	$\beta^-$ (M <sup>-1</sup> )	Source	Method
LiPF <sub>6</sub>	4	1.284	4.13	1.294	[87]	Molecular dynamics
LiPF <sub>6</sub>	2.63	2.119	4.75	2.299	[15]	Molecular dynamics
LiPF <sub>6</sub>	25.82	2.856	25.82	2.856	[16,17,27]	Experiments
LiBF <sub>4</sub>	2.81	0.754	2.81	0.754	[88]	Experiments
LiClO <sub>4</sub>	2.36	0.375	2.36	0.375	[89]	Experiments

could potentially influence  $\beta$  values, often determined through fitting process based on experimental measurements and molecular dynamics simulations. Documented values, as tabulated in Table A.1, can be as high as  $\beta = 2.86 \text{ M}^{-1}$  [16,17,27].

In Fig. A.2a, the diffusivity versus concentration for different  $\beta$  values suggest a significant deviation from Sand's constant diffusivity assumption, particularly at higher  $\beta$  values. Let us consider a scenario in electroplating where, for a system with a bulk salt concentration of  $c_0 = 1 \text{ M}$  and high dependency factor  $\beta = 2.86 \text{ M}^{-1}$ , ion depletion occurs due to the application of an over-limiting current density. Under this circumstance, the diffusivity varies from its bulk value,  $D_0 e^{-2.86} \approx 0.057 D_0$ , to the infinitely dilute value,  $D_0$ , as ions deplete at the anode surface, resulting in a 17-fold variation in ion diffusivity. This significant variation in diffusivity challenges the underlying assumption of constant electrolyte diffusivity in Sand's model.

As illustrated in Fig. A.2b the limiting current density  $i_{lim}$  (derived from Eq. (A.11)) versus  $\beta$  for various bulk concentrations  $c_0$ , we found the discrepancy between  $i_{lim}$  and the Sand's limiting current  $i_{lim}^*$  becomes pronounced at high concentrations and higher  $\beta$  values. We plot in Fig. A.3 the steady-state concentration profiles across the electrolyte for various current densities with three  $\beta$  values:  $\beta = 0 \text{ M}^{-1}$  in (a),  $\beta = 1 \text{ M}^{-1}$  in (b) and  $\beta = 2 \text{ M}^{-1}$  in (c). The results emphasize that the concentration distribution is significantly affected by  $\beta$ . While the concentration scales linearly with  $y$  in Sand's model (i.e.,  $\beta = 0 \text{ M}^{-1}$ ), our analytical solution in Eq. (A.9) predicts, for non-zero  $\beta$  values, a nonlinear, logarithmic distribution.

Overall, our analysis results suggest that ion transport dynamics, in terms of ion diffusivity, can vary significantly across the electrolyte during plating, especially under high current densities. The observed deviation in limiting current density and concentration profiles from Sand's predictions is due to the overlook of concentration's influence on diffusivity in the classical Sand's model.

## Appendix B. Supplementary data

Supplementary material related to this article can be found online at <https://doi.org/10.1016/j.est.2024.112615>.

## References

- [1] J.-M. Tarascon, M. Armand, Issues and challenges facing rechargeable lithium batteries, *Nature* 414 (6861) (2001) 359–367.
- [2] W. Xu, J. Wang, F. Ding, X. Chen, E. Nasybulin, Y. Zhang, J.-G. Zhang, Lithium metal anodes for rechargeable batteries, *Energy Environ. Sci.* 7 (2) (2014) 513–537.
- [3] R. Wang, W. Cui, F. Chu, F. Wu, Lithium metal anodes: Present and future, *J. Energy Chem.* 48 (2020) 145–159.
- [4] M. Gao, H. Li, L. Xu, Q. Xue, X. Wang, Y. Bai, C. Wu, Lithium metal batteries for high energy density: Fundamental electrochemistry and challenges, *J. Energy Chem.* 59 (2021) 666–687.
- [5] X. Xu, S. Wang, H. Wang, B. Xu, C. Hu, Y. Jin, J. Liu, H. Yan, The suppression of lithium dendrite growth in lithium sulfur batteries: A review, *J. Energy Storage* 13 (2017) 387–400.
- [6] M. Qi, L. Xie, Q. Han, L. Zhu, L. Chen, X. Cao, An overview of the key challenges and strategies for lithium metal anodes, *J. Energy Storage* 47 (2022) 103641.
- [7] P. Barai, K. Higa, V. Srinivasan, Lithium dendrite growth mechanisms in polymer electrolytes and prevention strategies, *Phys. Chem. Chem. Phys.* 19 (31) (2017) 20493–20505.
- [8] P. Zou, Y. Sui, H. Zhan, C. Wang, H.L. Xin, H.-M. Cheng, F. Kang, C. Yang, Polymorph evolution mechanisms and regulation strategies of lithium metal anode under multiphysical fields, *Chem. Rev.* 121 (10) (2021) 5986–6056.
- [9] P. Bai, J. Guo, M. Wang, A. Kushima, L. Su, J. Li, F.R. Brushett, M.Z. Bazant, Interactions between lithium growths and nanoporous ceramic separators, *Joule* 2 (11) (2018) 2434–2449.
- [10] A. Jana, S.I. Woo, K. Vikrant, R.E. García, Electrochemomechanics of lithium dendrite growth, *Energy Environ. Sci.* 12 (12) (2019) 3595–3607.
- [11] M. Rosso, C. Brissot, A. Teyssot, M. Dollé, L. Sannier, J.-M. Tarascon, R. Bouchet, S. Lascaud, Dendrite short-circuit and fuse effect on Li/polymer/Li cells, *Electrochim. Acta* 51 (25) (2006) 5334–5340.
- [12] C. Brissot, M. Rosso, J.-N. Chazalviel, S. Lascaud, Dendritic growth mechanisms in lithium/polymer cells, *J. Power Sources* 81 (1999) 925–929.
- [13] J. Landesfeind, H.A. Gasteiger, Temperature and concentration dependence of the ionic transport properties of lithium-ion battery electrolytes, *J. Electrochem. Soc.* 166 (14) (2019) A3079–A3097.
- [14] S. Mareev, D.Y. Butylskii, A. Kovalenko, A. Petukhova, N. Pismenskaya, L. Dammak, C. Larchet, V. Nikonenko, Accounting for the concentration dependence of electrolyte diffusion coefficient in the Sand and the Peers equations, *Electrochim. Acta* 195 (2016) 85–93.
- [15] B. Ravikumar, M. Mynam, B. Rai, Effect of salt concentration on properties of lithium ion battery electrolytes: A molecular dynamics study, *J. Phys. Chem. C* 122 (15) (2018) 8173–8181.
- [16] S.G. Stewart, J. Newman, The use of UV/vis absorption to measure diffusion coefficients in LiPF<sub>6</sub> electrolytic solutions, *J. Electrochem. Soc.* 155 (1) (2007) F13.
- [17] R. Akolkar, Mathematical model of the dendritic growth during lithium electrodeposition, *J. Power Sources* 232 (2013) 23–28.
- [18] Y. Ma, F. Wu, N. Chen, Y. Ma, C. Yang, Y. Shang, H. Liu, L. Li, R. Chen, Reversing the dendrite growth direction and eliminating the concentration polarization via an internal electric field for stable lithium metal anodes, *Chem. Sci.* 13 (32) (2022) 9277–9284.
- [19] J. Xiao, How lithium dendrites form in liquid batteries, *Science* 366 (6464) (2019) 426–427.
- [20] P. Bai, J. Li, F.R. Brushett, M.Z. Bazant, Transition of lithium growth mechanisms in liquid electrolytes, *Energy Environ. Sci.* 9 (10) (2016) 3221–3229.
- [21] J.-N. Chazalviel, Electrochemical aspects of the generation of ramified metallic electrodeposits, *Phys. Rev. A* 42 (12) (1990) 7355.
- [22] S.U. Kim, V. Srinivasan, A method for estimating transport properties of concentrated electrolytes from self-diffusion data, *J. Electrochem. Soc.* 163 (14) (2016) A2977.
- [23] C.-H. Chen, C.-W. Pao, Phase-field study of dendritic morphology in lithium metal batteries, *J. Power Sources* 484 (2021) 229203.
- [24] H.-J. Chang, A.J. Iltott, N.M. Trease, M. Mohammadi, A. Jerschow, C.P. Grey, Correlating microstructural lithium metal growth with electrolyte salt depletion in lithium batteries using 7Li MRI, *J. Am. Chem. Soc.* 137 (48) (2015) 15209–15216.
- [25] R.N. Wasalathanthri, R. Akolkar, Perspective—Does the sand equation reliably predict the onset of morphological evolution in lithium electrodeposition? *J. Electrochem. Soc.* 169 (9) (2022) 092519.
- [26] A. Mistry, V. Srinivasan, On our limited understanding of electrodeposition, *MRS Adv.* 4 (51–52) (2019) 2843–2861.
- [27] I.V. Thorat, D.E. Stephenson, N.A. Zacharias, K. Zaghib, J.N. Harb, D.R. Wheeler, Quantifying tortuosity in porous Li-ion battery materials, *J. Power Sources* 188 (2) (2009) 592–600.
- [28] J.W. Cahn, J.E. Hilliard, Free energy of a nonuniform system. I. Interfacial free energy, *J. Chem. Phys.* 28 (2) (1958) 258–267.
- [29] C.-J. Ko, C.-H. Chen, K.-C. Chen, Influence of inhomogeneity of lithium-ion transport within the anode/electrolyte interface on mossy lithium formation, *J. Power Sources* 563 (2023) 232779.
- [30] S.-J. Chang, C.-H. Chen, K.-C. Chen, Assessment of the mechanical suppression of nonuniform electrodeposition in lithium metal batteries, *Phys. Chem. Chem. Phys.* 24 (18) (2022) 11086–11095.
- [31] L. Chen, H.W. Zhang, L.Y. Liang, Z. Liu, Y. Qi, P. Lu, J. Chen, L.-Q. Chen, Modulation of dendritic patterns during electrodeposition: A nonlinear phase-field model, *J. Power Sources* 300 (2015) 376–385.
- [32] L. Liang, L.-Q. Chen, Nonlinear phase field model for electrodeposition in electrochemical systems, *Appl. Phys. Lett.* 105 (26) (2014) 263903.
- [33] V. Yurkiv, T. Foroozan, A. Ramasubramanian, R. Shahbazian-Yassar, F. Mashayek, Phase-field modeling of Solid Electrolyte Interface (SEI) influence on Li dendritic behavior, *Electrochim. Acta* 265 (2018) 609–619.
- [34] Z. Hong, V. Viswanathan, Phase-field simulations of lithium dendrite growth with open-source software, *ACS Energy Lett.* 3 (7) (2018) 1737–1743.

- [35] W. Mu, X. Liu, Z. Wen, L. Liu, Numerical simulation of the factors affecting the growth of lithium dendrites, *J. Energy Storage* 26 (2019) 100921.
- [36] R. Zhang, X. Shen, Y.-T. Zhang, X.-L. Zhong, H.-T. Ju, T.-X. Huang, X. Chen, J.-D. Zhang, J.-Q. Huang, Dead lithium formation in lithium metal batteries: A phase field model, *J. Energy Chem.* 71 (2022) 29–35.
- [37] R. Zhang, X. Shen, H.-T. Ju, J.-D. Zhang, Y.-T. Zhang, J.-Q. Huang, Driving lithium to deposit inside structured lithium metal anodes: A phase field model, *J. Energy Chem.* 73 (2022) 285–291.
- [38] M.E. Arguello, M. Gumulya, J. Derksen, R. Utikar, V.M. Calo, Phase-field modeling of planar interface electrodeposition in lithium-metal batteries, *J. Energy Storage* 50 (2022) 104627.
- [39] M.E. Arguello, N.A. Labanda, V.M. Calo, M. Gumulya, R. Utikar, J. Derksen, Dendrite formation in rechargeable lithium-metal batteries: Phase-field modeling using open-source finite element library, *J. Energy Storage* 53 (2022) 104892.
- [40] D. Han, C. Lin, Numerical study of the formation of dead lithium during cycling and the mechanism of its effect on battery performance, *J. Energy Storage* 83 (2024) 110641.
- [41] M.E. Arguello, N.A. Labanda, V.M. Calo, M. Gumulya, R. Utikar, J. Derksen, Three-dimensional experimental-scale phase-field modeling of dendrite formation in rechargeable lithium-metal batteries, *J. Energy Storage* 62 (2023) 106854.
- [42] J.-Y. Li, C.-H. Lei, L.-J. Li, Y.-C. Shu, Y.-Y. Liu, Unconventional phase field simulations of transforming materials with evolving microstructures, *Acta Mech. Sinica* 28 (2012) 915–927.
- [43] Y. Shu, J. Yen, Multivariant model of martensitic microstructure in thin films, *Acta Mater.* 56 (2008) 3969–3981.
- [44] A. Karma, Phase-field formulation for quantitative modeling of alloy solidification, *Phys. Rev. Lett.* 87 (11) (2001) 115701.
- [45] L. Eastgate, J. Sethna, M. Rauscher, T. Cretegn, C.-S. Chen, C. Myers, Fracture in mode I using a conserved phase-field model, *Phys. Rev. E* 65 (3) (2002) 036117.
- [46] V. Hakim, A. Karma, Laws of crack motion and phase-field models of fracture, *J. Mech. Phys. Solids* 57 (2) (2009) 342–368.
- [47] A.J. Pons, A. Karma, Helical crack-front instability in mixed-mode fracture, *Nature* 464 (7285) (2010) 85–89.
- [48] C.-H. Chen, T. Cambon, V. Lazarus, M. Nicoli, A.J. Pons, A. Karma, Crack front segmentation and facet coarsening in mixed-mode fracture, *Phys. Rev. Lett.* 115 (26) (2015) 265503.
- [49] C.-H. Chen, E. Bouchbinder, A. Karma, Instability in dynamic fracture and the failure of the classical theory of cracks, *Nat. Phys.* 13 (12) (2017) 1186.
- [50] Y. Lubomirsky, C.-H. Chen, A. Karma, E. Bouchbinder, Universality and stability phase diagram of two-dimensional brittle fracture, *Phys. Rev. Lett.* 121 (13) (2018) 134301.
- [51] C.-Y. Chen, H.-J. Wu, Numerical simulations of interfacial instabilities on a rotating miscible magnetic droplet with effects of Korteweg stresses, *Phys. Fluids* 17 (4) (2005) 042101.
- [52] C.-Y. Chen, C.-H. Chen, J.A. Miranda, Numerical study of pattern formation in miscible rotating Hele-Shaw flows, *Phys. Rev. E* 73 (4) (2006) 046306.
- [53] C.-Y. Chen, Y.-S. Huang, J.A. Miranda, Diffuse-interface approach to rotating Hele-Shaw flows, *Phys. Rev. E* 84 (4) (2011) 046302.
- [54] D.A. Cogswell, Quantitative phase-field modeling of dendritic electrodeposition, *Phys. Rev. E* 92 (1) (2015) 011301.
- [55] D.R. Ely, A. Jana, R.E. García, Phase field kinetics of lithium electrodeposits, *J. Power Sources* 272 (2014) 581–594.
- [56] W.J. Boettinger, J.A. Warren, C. Beckermann, A. Karma, Phase-field simulation of solidification, *Annu. Rev. Mater. Res.* 32 (1) (2002) 163–194.
- [57] Q. Cheng, L. Wei, Z. Liu, N. Ni, Z. Sang, B. Zhu, W. Xu, M. Chen, Y. Miao, L.-Q. Chen, et al., Operando and three-dimensional visualization of anion depletion and lithium growth by stimulated Raman scattering microscopy, *Nature Commun.* 9 (1) (2018) 2942.
- [58] J. Elezgaray, C. Léger, F. Argoul, Linear stability analysis of unsteady galvanostatic electrodeposition in the two-dimensional diffusion-limited regime, *J. Electrochem. Soc.* 145 (6) (1998) 2016.
- [59] Z. Peng, X. Cao, P. Gao, H. Jia, X. Ren, S. Roy, Z. Li, Y. Zhu, W. Xie, D. Liu, et al., High-power lithium metal batteries enabled by high-concentration acetonitrile-based electrolytes with vinylene carbonate additive, *Adv. Funct. Mater.* 30 (24) (2020) 2001285.
- [60] R. Akolkar, Modeling dendrite growth during lithium electrodeposition at sub-ambient temperature, *J. Power Sources* 246 (2014) 84–89.
- [61] J. Tan, E.M. Ryan, Computational study of electro-convection effects on dendrite growth in batteries, *J. Power Sources* 323 (2016) 67–77.
- [62] M. Ota, S. Izuo, K. Nishikawa, Y. Fukunaka, E. Kusaka, R. Ishii, J. Selman, Measurement of concentration boundary layer thickness development during lithium electrodeposition onto a lithium metal cathode in propylene carbonate, *J. Electroanal. Chem.* 559 (2003) 175–183.
- [63] G. Liu, W. Lu, A model of concurrent lithium dendrite growth, SEI growth, SEI penetration and regrowth, *J. Electrochem. Soc.* 164 (9) (2017) A1826–A1833.
- [64] J. Christensen, P. Albertus, R.S. Sanchez-Carrera, T. Lohmann, B. Kozinsky, R. Liedtke, J. Ahmed, A. Kojic, A critical review of Li/Air batteries, *J. Electrochem. Soc.* 159 (2) (2011) R1.
- [65] L. Porz, T. Swamy, B.W. Sheldon, D. Rettenwander, T. Frömling, H.L. Thaman, S. Berends, R. Uecker, W.C. Carter, Y.-M. Chiang, Mechanism of lithium metal penetration through inorganic solid electrolytes, *Adv. Energy Mater.* 7 (20) (2017) 1701003.
- [66] K.N. Wood, E. Kazyak, A.F. Chadwick, K.-H. Chen, J.-G. Zhang, K. Thornton, N.P. Dasgupta, Dendrites and pits: Untangling the complex behavior of lithium metal anodes through operando video microscopy, *ACS Central Sci.* 2 (11) (2016) 790–801.
- [67] X. Lin, J. Park, L. Liu, Y. Lee, A. Sastry, W. Lu, A comprehensive capacity fade model and analysis for Li-ion batteries, *J. Electrochem. Soc.* 160 (10) (2013) A1701–A1710.
- [68] L.T. Le, T.D. Vo, K.H. Ngo, S. Okada, F. Alloin, A. Garg, P.M. Le, Mixing ionic liquids and ethylene carbonate as safe electrolytes for lithium-ion batteries, *J. Mol. Liq.* 271 (2018) 769–777.
- [69] A. Kushima, K.P. So, C. Su, P. Bai, N. Kuriyama, T. Maebashi, Y. Fujiwara, M.Z. Bazant, J. Li, Liquid cell transmission electron microscopy observation of lithium metal growth and dissolution: Root growth, dead lithium and lithium flotsams, *Nano Energy* 32 (2017) 271–279.
- [70] M.B. Pinson, M.Z. Bazant, Theory of SEI formation in rechargeable batteries: Capacity fade, accelerated aging and lifetime prediction, *J. Electrochem. Soc.* 160 (2) (2013) A243–A250.
- [71] H.J. Ploehn, P. Ramadass, R.E. White, Solvent diffusion model for aging of lithium-ion battery cells, *J. Electrochem. Soc.* 151 (3) (2004) A456–A462.
- [72] M. Doyle, J. Newman, A.S. Gozdz, C.N. Schmutz, J.-M. Tarascon, Comparison of modeling predictions with experimental data from plastic lithium ion cells, *J. Electrochem. Soc.* 143 (6) (1996) 1890–1903.
- [73] M. Van Soestbergen, P. Biesheuvel, M.Z. Bazant, Diffuse-charge effects on the transient response of electrochemical cells, *Phys. Rev. E* 81 (2) (2010) 021503.
- [74] T.K. Schwietert, P. Ombrini, L.S. Ootes, L. Oostrum, V. Azizi, D. Cogswell, J. Zhu, M.Z. Bazant, M. Wagemaker, A. Vasiladiadis, Phase-field computational framework for addressing challenges in solid-state batteries, *PRX Energy* 2 (3) (2023) 033014.
- [75] E. Peled, S. Menkin, SEI: Past, present and future, *J. Electrochem. Soc.* 164 (7) (2017) A1703.
- [76] K. Xu, Nonaqueous liquid electrolytes for lithium-based rechargeable batteries, *Chem. Rev.* 104 (10) (2004) 4303–4418.
- [77] X.-B. Cheng, R. Zhang, C.-Z. Zhao, F. Wei, J.-G. Zhang, Q. Zhang, A review of solid electrolyte interphases on lithium metal anode, *Adv. Sci.* 3 (3) (2016) 1500213.
- [78] K.N. Wood, M. Noked, N.P. Dasgupta, Lithium metal anodes: Toward an improved understanding of coupled morphological, electrochemical, and mechanical behavior, *ACS Energy Letters* 2 (3) (2017) 664–672.
- [79] G.G. Stoney, The tension of metallic films deposited by electrolysis, *Proc. R. Soc. Lond. Ser. A* 82 (553) (1909) 172–175.
- [80] Y. Liu, K. Guo, C. Wang, H. Gao, Wrinkling and ratcheting of a thin film on cyclically deforming plastic substrate: mechanical instability of the solid-electrolyte interphase in li-ion batteries, *J. Mech. Phys. Solids* 123 (2019) 103–118.
- [81] M.K. Jangid, A. Mukhopadhyay, Real-time monitoring of stress development during electrochemical cycling of electrode materials for li-ion batteries: overview and perspectives, *J. Mater. Chem. A* 7 (41) (2019) 23679–23726.
- [82] K. Dokko, D. Watanabe, Y. Ugata, M.L. Thomas, S. Tsuzuki, W. Shinoda, K. Hashimoto, K. Ueno, Y. Umebayashi, M. Watanabe, Direct evidence for Li ion hopping conduction in highly concentrated sulfolane-based liquid electrolytes, *J. Phys. Chem. B* 122 (47) (2018) 10736–10745.
- [83] Y. Ugata, M.L. Thomas, T. Mandai, K. Ueno, K. Dokko, M. Watanabe, Li-ion hopping conduction in highly concentrated lithium bis (fluorosulfonyl) amide/dinitrile liquid electrolytes, *Phys. Chem. Chem. Phys.* 21 (19) (2019) 9759–9768.
- [84] A. Maraschky, R. Akolkar, Mechanism explaining the onset time of dendritic lithium electrodeposition via considerations of the Li<sup>+</sup> transport within the solid electrolyte interphase, *J. Electrochem. Soc.* 165 (14) (2018) D696.
- [85] C. Yan, H. Yuan, H.S. Park, J.-Q. Huang, Perspective on the critical role of interface for advanced batteries, *J. Energy Chem.* 47 (2020) 217–220.
- [86] H.J. Sand, III, on the concentration at the electrodes in a solution, with special reference to the liberation of hydrogen by electrolysis of a mixture of copper sulphate and sulphuric acid, *The London, Edinburgh, and Dublin Philosophical Magazine and Journal of Science* 1 (1) (1901) 45–79.
- [87] H. Haghighi, B. Ghalami Choobar, S. Amjad-iranagh, Effect of salt concentration on properties of mixed carbonate-based electrolyte for Li-ion batteries: A molecular dynamics simulation study, *Journal of Molecular Modeling* 26 (2020) 1–15.
- [88] P. Richardson, A. Voice, I. Ward, Pulsed-field gradient NMR self diffusion and ionic conductivity measurements for liquid electrolytes containing LiBF<sub>4</sub> and propylene carbonate, *Electrochim. Acta* 130 (2014) 606–618.
- [89] A. Ehrl, J. Landesfeind, W.A. Wall, H.A. Gasteiger, Determination of transport parameters in liquid binary lithium ion battery electrolytes, *J. Electrochem. Soc.* 164 (4) (2017) A826.